

SAR Imaging on HEO Satellites with an Improved Frequency-Domain Algorithm

Po-Chih Chen and Jean-Fu Kiang*

Abstract—The possibility of employing highly-elliptical-orbit (HEO) satellites for SAR imaging is investigated. A constellation of two satellites in the Tundra orbits, which are capable of covering all the high-latitude areas, are chosen as the platforms for SAR imaging. The received signal is processed with an improved frequency-domain algorithm (FDA) to reconstruct the image. Simulation results verify that the proposed method can produce better SAR images with less computational load and memory than the conventional FDA.

1. INTRODUCTION

Geosynchronous (GEO) satellites have been used for radio/TV broadcast, weather monitoring [1–3] and image processing [4–10]. Compared with medium-earth-orbit (MEO) and low-earth-orbit (LEO) satellites, the GEO satellites have the advantages of wider coverage, longer life-time, lower gateway cost and higher stability. The orbit of a GEO satellite is close to a complete circle, leading to steady free-space loss and link budget. However, GEO satellites require higher transmission power, while producing images with relatively poorer resolution.

Highly-elliptical-orbit (HEO) satellites have been used for communications over high-latitude areas, where signals from GEO satellites are frequently blocked by the terrains [11]. Typically, a number of satellites are deployed on complementary orbits to provide complete coverage over a specific area [11]. Satellites were employed on the Molniya and the Tundra orbits [12–16] by the former Soviet Union, for TV broadcast to high-latitude cities. A constellation of three satellites can be deployed in a Molniya orbit to provide continuous coverage at a specific longitude. Each satellite has a 12-hour period and is operational over an 8-hour window around the apogee. Similar coverage can be provided to a point on the ground in the same hemisphere but 180° of longitude apart. For example, the same Molniya orbit can provide good coverage to both Siberia and North America. The apogee of a Tundra orbit lies at almost twice the altitude of a GEO orbit. The period of satellites on a Tundra orbit is 24 hours, and only two satellites are required to provide continuous coverage to a specific area, with each operating for 12 hours.

In this work, HEO satellites are envisioned as platforms for SAR imaging. A constellation of two satellites in the Tundra orbit are simulated to detect a point target on the ground. In such a HEO SAR mission, the Doppler centroid is extremely large when the satellite is far away from the apogee, due to high eccentricity of the orbit. Thus, a large number of azimuth samples are required to obtain an image with compatible resolution to that achieved in a low-squint mode. In addition, the difference between the maximum and the minimum distances between the satellite and the target area is extremely large, demanding a much larger number of range samples than that in a low-squint mode. As a result, the computational load and the memory size are significantly increased. To resolve all these issues, a modified frequency-domain algorithm (FDA), suitable for high-squint SAR imaging, is proposed to

Received 13 January 2017, Accepted 28 February 2017, Scheduled 9 April 2017

* Corresponding author: Jean-Fu Kiang (jfkang@ntu.edu.tw).

The authors are with the Graduate Institute of Communication Engineering, National Taiwan University, Taipei, Taiwan, R.O.C.

support the envisioned HEO SAR missions, which takes much lower computational load and memory size than those demanded by the conventional FDA.

This paper is organized as follows. The proposed method is presented in Section 2, and the satellite orbit and ephemeris are briefly reviewed in Section 3. Simulation results, including the image quality as well as the computational load and memory size, over six mission events are discussed in Section 4. Finally, some conclusions are drawn in Section 5.

2. PROPOSED METHOD

Figure 1 shows a flowchart of the proposed method for high-squint SAR imaging, which is similar to the conventional FDA [4], and the processes different from those in the latter are enclosed with parentheses. The received baseband signal is rotated in the τ - η plane before being Fourier transformed to the f_τ - f_η plane. The reference function multiply (RFM) filter is rotated in the f_τ - f_η plane with the same angle. Finally, the processed signal is reversely rotated in the τ - η plane to form the final image.

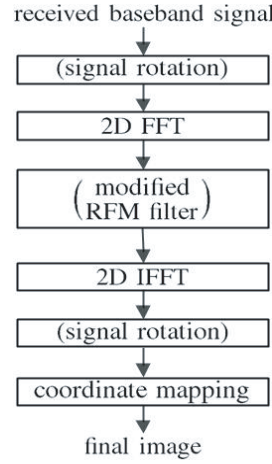


Figure 1. Flowchart of proposed method for high-squint SAR imaging. The processes enclosed with parentheses are different from those in the conventional FDA [4].

The received baseband signal can be represented as

$$s_{\text{rb}}(\tau, \eta) = A_0(x, y)w_e(\tau - 2R_s(\eta, x, y)/c)e^{-j4\pi f_0 R_s(\eta, x, y)/c + j\pi K_r[\tau - 2R_s(\eta, x, y)/c]^2} \quad (1)$$

where τ is the range (fast) time; $A_0(x, y)$ is a complex amplitude associated with the scattering amplitude of a point target at $(x, y, 0)$; f_0 is the carrier frequency, c is the speed of the light; K_r is the FM rate of the LFM pulse with duration T_r ; $w_e(\tau) = \text{rect}(\tau/T_r)$ is the range window with duration T_r ; $\text{rect}(\tau)$ is a rectangular function defined as

$$\text{rect}(\tau) = \begin{cases} 1, & |\tau| \leq 1/2 \\ 0, & \text{otherwise} \end{cases} \quad (2)$$

The received baseband signal is stored in a matrix of dimension $N_a \times N_r$, where the azimuth sampling number (N_a) determines the resolution in the azimuthal direction, and the range sampling number (N_r) should be large enough to record all the echoed signals from the target area. For the convenience of applying the fast Fourier transform (FFT) algorithm, both N_a and N_r are incremented, respectively, to the nearest integers that are powers of two.

2.1. Rotation in τ - η Plane

Figures 2(a) and 2(b) show the schematic of the received baseband signal in the coordinates $(\tau - \tau_0, \eta)$ and $(\tau' - \tau_0, \eta')$, respectively, where $\tau_0 = 2R_{s0}/c$ and R_{s0} is the distance from the center point of the flight path to the beam center point (BCP) on the ground. As shown in Fig. 2(b), the number of range

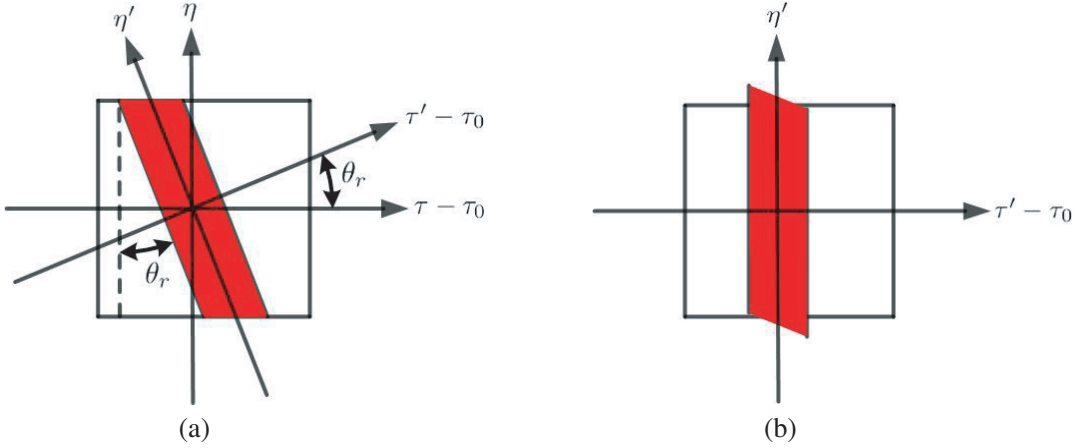


Figure 2. Schematic of received baseband signal represented in coordinates (a) $(\tau - \tau_0, \eta)$ and (b) $(\tau' - \tau_0, \eta')$.

samples has been significantly reduced in the coordinates of $(\tau' - \tau_0, \eta')$. The rotation angle θ_r between these two coordinate systems is determined as $\theta_r = \tan^{-1} \frac{2D/c}{L/V_p}$, where L is the total length of the flight path, and D is the length difference between the line segments that connect the BCP to the starting point and the ending point, respectively, of the flight path. Explicitly, these two coordinate systems are related as

$$\begin{bmatrix} \tau - \tau_0 \\ \eta \end{bmatrix} = \begin{bmatrix} \cos \theta_r & -\sin \theta_r \\ \sin \theta_r & \cos \theta_r \end{bmatrix} \begin{bmatrix} \tau' - \tau_0 \\ \eta' \end{bmatrix} = \begin{bmatrix} (\tau' - \tau_0) \cos \theta_r - \eta' \sin \theta_r \\ (\tau' - \tau_0) \sin \theta_r + \eta' \cos \theta_r \end{bmatrix} \quad (3)$$

or

$$\begin{bmatrix} \tau \\ \eta \end{bmatrix} = \begin{bmatrix} (\tau' - \tau_0) \cos \theta_r - \eta' \sin \theta_r + \tau_0 \\ (\tau' - \tau_0) \sin \theta_r + \eta' \cos \theta_r \end{bmatrix} = \begin{bmatrix} g(\tau', \eta') \\ h(\tau', \eta') \end{bmatrix}$$

The received baseband-signal originally stored with respect to the (τ, η) coordinates can be represented in the (τ', η') coordinates as

$$s_{rb}(\tau', \eta') = s_{rb}(\tau, \eta) \Big|_{\tau=g(\tau', \eta'), \eta=h(\tau', \eta')} \quad (4)$$

which are stored in a matrix of dimension $N'_a \times N'_r$. For the convenience of applying the FFT algorithm, both N'_a and N'_r are incremented, respectively, to the nearest integers that are powers of two. Without loss of generality, we choose $\Delta\tau' = \Delta\tau$ and $\Delta\eta' = \Delta\eta$.

2.2. DRM-5

The slant range in a GEO SAR mission can be represented as [4]

$$R_s(\eta) = |\bar{r}_s(\eta) - \bar{r}_g(\eta)| \quad (5)$$

where $\bar{r}_s(\eta)$ and $\bar{r}_g(\eta)$ are the positions of the satellite and the target, respectively, at azimuth time η . Define

$$\begin{aligned} \bar{R}(\eta) &= \bar{r}_s(\eta) - \bar{r}_g(\eta), & \bar{V}(\eta) &= \frac{d\bar{R}(\eta)}{d\eta} = \bar{v}_s(\eta) - \bar{v}_g(\eta) \\ \bar{A}(\eta) &= \frac{d\bar{V}(\eta)}{d\eta} = \bar{a}_s(\eta) - \bar{a}_g(\eta), & \bar{B}(\eta) &= \frac{d\bar{A}(\eta)}{d\eta} = \bar{b}_s(\eta) - \bar{b}_g(\eta) \\ \bar{D}(\eta) &= \frac{d\bar{B}(\eta)}{d\eta} = \bar{d}_s(\eta) - \bar{d}_g(\eta), & \bar{E}(\eta) &= \frac{d\bar{D}(\eta)}{d\eta} = \bar{e}_s(\eta) - \bar{e}_g(\eta) \end{aligned}$$

where $\bar{v}_s(\eta)$ and $\bar{v}_g(\eta)$ are the velocity vectors of the satellite and the target, respectively, at azimuth time η ; $\bar{a}_s(\eta)$ and $\bar{a}_g(\eta)$ are the satellite acceleration vector and the target acceleration vector, respectively; $\bar{b}_s(\eta)$ and $\bar{b}_g(\eta)$ are the time derivatives of $\bar{a}_s(\eta)$ and $\bar{a}_g(\eta)$, respectively; $\bar{d}_s(\eta)$ and $\bar{d}_g(\eta)$ are the time derivatives of $\bar{b}_s(\eta)$ and $\bar{b}_g(\eta)$, respectively; $\bar{e}_s(\eta)$ and $\bar{e}_g(\eta)$ are the time derivatives of $\bar{d}_s(\eta)$ and $\bar{d}_g(\eta)$, respectively; all at azimuth time η . A fifth-order Doppler parameter range model (DRM-5) is represented as [4].

$$R_s(\eta) = R_c + \sum_{n=1}^5 k_n \eta^n \quad (6)$$

where $R_c = |\bar{R}(0)|$ is the slant range at $\eta = 0$, and

$$\begin{aligned} k_1 &= \frac{\bar{R}^t(0) \cdot \bar{V}(0)}{|\bar{R}(0)|}, & k_2 &= \frac{\bar{R}^t(0) \cdot \bar{A}(0) + \bar{V}^t(0) \cdot \bar{V}(0) - k_1^2}{2|\bar{R}(0)|} \\ k_3 &= \frac{\bar{R}^t(0) \cdot \bar{B}(0) + 3\bar{V}^t(0) \cdot \bar{A}(0) - 6k_1k_2}{6|\bar{R}(0)|} \\ k_4 &= \frac{\bar{R}^t(0) \cdot \bar{D}(0) + 4\bar{V}^t(0) \cdot \bar{B}(0) + 3\bar{A}^t(0) \cdot \bar{A}(0)}{24|\bar{R}(0)|} - \frac{k_2^2 + 2k_1k_3}{2|\bar{R}(0)|} \\ k_5 &= \frac{\bar{R}^t(0) \cdot \bar{E}(0) + 5\bar{V}^t(0) \cdot \bar{D}(0) + 10\bar{A}^t(0) \cdot \bar{B}(0)}{120|\bar{R}(0)|} - \frac{k_2k_3 + k_1k_4}{|\bar{R}(0)|} \end{aligned}$$

2.3. Modified RFM Filter

The RFM filter used in the conventional FDA is represented as [4]

$$H_{\text{RFM}}(f_\tau, f_\eta) = e^{-j[\phi_r(f_\tau) + \phi_{\text{RCM}}(f_\tau, f_\eta) + \phi_a(f_\eta) + \phi_c(f_\tau, f_\eta)]} \quad (7)$$

where $\phi_r(f_\tau)$, $\phi_{\text{RCM}}(f_\tau, f_\eta)$, $\phi_a(f_\eta)$ and $\phi_c(f_\tau, f_\eta)$ are the phases to conduct range compression, range cell migration (RCM) correction, azimuth compression and decoupling, respectively. Their explicit forms are

$$\begin{aligned} \phi_r(f_\tau) &= -\frac{\pi f_\tau^2}{K_r} \\ \phi_{\text{RCM}}(f_\tau, f_\eta) &= -\frac{4\pi f_\tau}{c} \left\{ R_c + \frac{\lambda_0^2 A_1}{8} [2f_{\text{dc}}(f_\eta - f_{\text{dc}}) + (f_\eta - f_{\text{dc}})^2] - \frac{\lambda_0^3 A_2}{24} [3f_{\text{dc}}(f_\eta - f_{\text{dc}})^2 + 2(f_\eta - f_{\text{dc}})^3] \right. \\ &\quad \left. + \frac{\lambda_0^4 A_3}{64} [4f_{\text{dc}}(f_\eta - f_{\text{dc}})^3 + 3(f_\eta - f_{\text{dc}})^4] - \frac{\lambda_0^5 A_4}{160} [5f_{\text{dc}}(f_\eta - f_{\text{dc}})^4 + 4(f_\eta - f_{\text{dc}})^5] \right\} \\ \phi_a(f_\eta) &= -\frac{4\pi R_c}{\lambda_0} + \frac{\pi \lambda_0 A_1}{2} (f_\eta - f_{\text{dc}})^2 - \frac{\pi \lambda_0^2 A_2}{6} (f_\eta - f_{\text{dc}})^3 + \frac{\pi \lambda_0^3 A_3}{16} (f_\eta - f_{\text{dc}})^4 - \frac{\pi \lambda_0^4 A_4}{40} (f_\eta - f_{\text{dc}})^5 \\ \phi_c(f_\tau, f_\eta) &= \left(\frac{\pi f_\tau^2 f_\eta^2}{f_0^2} \right) \left\{ \frac{\lambda_0 A_1}{2} - \frac{\lambda_0^2 A_2}{2} (f_\eta - f_{\text{dc}}) + \frac{3\lambda_0^3 A_3}{8} (f_\eta - f_{\text{dc}})^2 - \frac{\lambda_0^4 A_4}{4} (f_\eta - f_{\text{dc}})^3 \right\} \\ &\quad + \left(\frac{\pi f_\tau^3 f_\eta^2}{f_0^3} \right) \left\{ -\frac{\lambda_0 A_1}{2} + \frac{\lambda_0^2 A_2}{6} [4(f_\eta - f_{\text{dc}}) + f_{\text{dc}}] - \frac{\lambda_0^3 A_3}{8} [5(f_\eta - f_{\text{dc}})^2 + 2f_{\text{dc}}(f_\eta - f_{\text{dc}})] \right. \\ &\quad \left. + \frac{\lambda_0^4 A_4}{4} [2(f_\eta - f_{\text{dc}})^3 + f_{\text{dc}}(f_\eta - f_{\text{dc}})^2] \right\} \end{aligned}$$

where

$$A_1 = \frac{1}{2k_2}, \quad A_2 = -\frac{3k_3}{8k_2^3}, \quad A_3 = \frac{9k_3^2 - 4k_2k_4}{16k_2^5}, \quad A_4 = -\frac{135k_3^3 - 120k_2k_3k_4 + 20k_2^2k_5}{128k_2^7}$$

Before applying the RFM filter, it is first rotated to the f'_τ - f'_η domain as [17]

$$H_{\text{RFM}}(f'_\tau, f'_\eta) = H_{\text{RFM}}(f_\tau, f_\eta) \Big|_{f_\tau=g_1(f'_\tau, f'_\eta), f_\eta=h_1(f'_\tau, f'_\eta)} \quad (8)$$

where the $(f_\tau, f_\eta - f_{\text{dc}})$ and the $(f'_\tau, f'_\eta - f_{\text{dc}})$ coordinates are related by the same rotation angle θ_r as

$$\begin{bmatrix} f_\tau \\ f_\eta - f_{\text{dc}} \end{bmatrix} = \begin{bmatrix} \cos \theta_r & -\sin \theta_r \\ \sin \theta_r & \cos \theta_r \end{bmatrix} \begin{bmatrix} f'_\tau \\ f'_\eta - f_{\text{dc}} \end{bmatrix} = \begin{bmatrix} f'_\tau \cos \theta_r - (f'_\eta - f_{\text{dc}}) \sin \theta_r \\ f'_\tau \sin \theta_r + (f'_\eta - f_{\text{dc}}) \cos \theta_r \end{bmatrix}$$

or

$$\begin{bmatrix} f_\tau \\ f_\eta \end{bmatrix} = \begin{bmatrix} f'_\tau \cos \theta_r - (f'_\eta - f_{\text{dc}}) \sin \theta_r \\ f'_\tau \sin \theta_r + (f'_\eta - f_{\text{dc}}) \cos \theta_r + f_{\text{dc}} \end{bmatrix} = \begin{bmatrix} g_1(f'_\tau, f'_\eta) \\ h_1(f'_\tau, f'_\eta) \end{bmatrix}$$

3. SATELLITE ORBIT AND EPHEMERIS

Table 1 lists the parameters of a Tundra orbit [12]. A constellation of two satellites are deployed to detect a point target specified in the Earth-centered Earth-fixed (ECEF) coordinate system. The right-of-ascending-node and true anomaly of the second satellite differ from those of the first one by 180° , and the other parameters are the same.

Figure 3 shows the ephemeris of the two Tundra satellites. The solid circle marks a point target randomly selected for testing. Along each ephemeris, the thick part marks the working period, which is centered around the apogee and lasts for half of the period.

Figure 4 shows the time history of squint angles (θ_s) measured from the two Tundra satellites. The period (T) of each Tundra satellite is 24 hours, and the first satellite passes the apogee at $t = 0$. Thus,

Table 1. Parameters of Tundra orbit [12].

parameter	symbol	magnitude	unit
semi-major axis	a	42,164	km
eccentricity	e	0.3	
right of ascending node	Ω	40	deg.
orbital inclination	i	63.4	deg.
argument of perigee	ω	270	deg.
true anomaly	ν	180	deg.

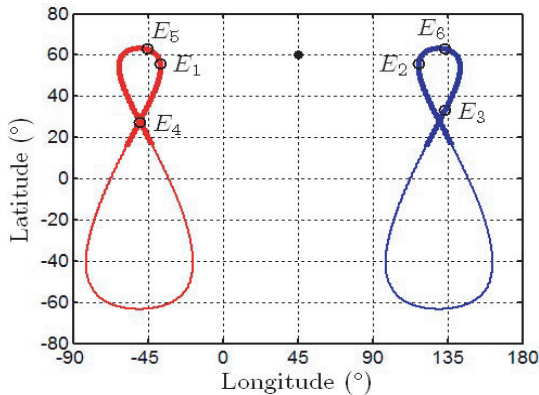


Figure 3. Ephemeris of two Tundra satellites, the solid circle marks a point target randomly selected for testing.

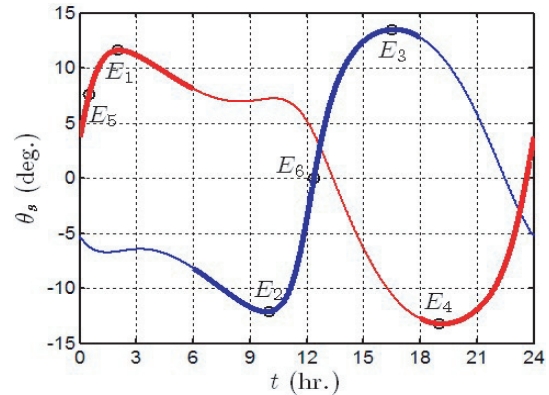


Figure 4. Time history of squint angles measured from the two Tundra satellites.

the first satellite operates in $0 < t < T/4$ and $3T/4 < t < T$, and the second one operates for the rest of the period.

4. SIMULATIONS AND DISCUSSIONS

Table 2 lists the parameters of a GEO SAR mission, which will be used for simulations in this work [4]. Table 3 lists the number of multiplications (NOMs) which are required by the proposed method and the conventional FDA, respectively. The memories required by the conventional FDA and the proposed method to store the received signal are on the order of $N_r \times N_a$ and $N'_r \times N'_a$, respectively.

Table 2. Parameters of a SAR mission [4].

parameter	symbol	magnitude	unit
carrier frequency	f_0	1.2	GHz
chirp pulse duration	T_r	50	μs
range chirp rate	K_r	620	GHz
bandwidth	B_r	31	MHz
range sampling rate	F_r	64 / 128*	MHz
range sampling interval	$\Delta\tau$	15.63 / 7.81*	ns
azimuth sampling rate	F_a	120 / 240*	Hz
azimuth sampling interval	$\Delta\eta$	8.33 / 4.17*	ms

a/b^* : a is used in Events E_1 - E_4 and b is used in Events E_5 , E_6 .

Table 3. Number of multiplications in algorithms.

operation	conventional FDA	proposed method
signal rotation	none	$4N'_r N'_a$
spectrum rotation	none	$4N'_r N'_a$
range FFT	$2N_r N_a \log_2 N_a$	$2N'_r N'_a \log_2 N'_a$
azimuth FFT	$2N_a N_r \log_2 N_r$	$2N'_a N'_r \log_2 N'_r$
$f_\tau^2, f_\tau^3, f_\eta^2$	$2N_r + N_a$	$3N'_r N'_a$
$(f_\eta - f_{dc})^2 - (f_\eta - f_{dc})^5$	$4N_a$	$4N'_r N'_a$
ϕ_r	N_r	$N'_r N'_a$
ϕ_{RCM}	$8N_a + N_r N_a$	$9N'_r N'_a$
ϕ_a	$4N_a$	$4N'_r N'_a$
ϕ_c	$12N_a + 2N_r N_a$	$14N'_r N'_a$
H_{RFM}	$2N_r N_a$	$2N'_r N'_a$
date blocking	none	none
residual phase compensation	none	none
range IFFT	$2N_r N_a \log_2 N_a$	$2N'_r N'_a \log_2 N'_a$
azimuth IFFT	$2N_a N_r \log_2 N_r$	$2N'_a N'_r \log_2 N'_r$
coordinate mapping	$N_a + N_r$	$2N'_r N'_a$

The SAR images of the target point are taken at six locations, marked as events E_1 - E_6 in Figs. 3 and 4. The four extreme events (E_1 - E_4) involve high squint angles, the moderate event (E_5) involves a small squint angle, and the non-squint event (E_6) involves a zero squint angle. Both the conventional

FDA and the proposed method are applied to reconstruct the images of the point target. The four extreme events are expected to impose more stringent challenges on applying the HEO satellites for SAR imaging. In each event, the responsible satellite is determined first, then both the conventional FDA and the proposed method are applied to reconstruct the image of the point target.

4.1. Event E_1

Figure 5(a) shows the received signal in the τ - η plane, which is computed by using Eq. (1). Fig. 5(b) shows the image reconstructed with the conventional FDA, in which local maxima are observed along the x axis and y' axis.

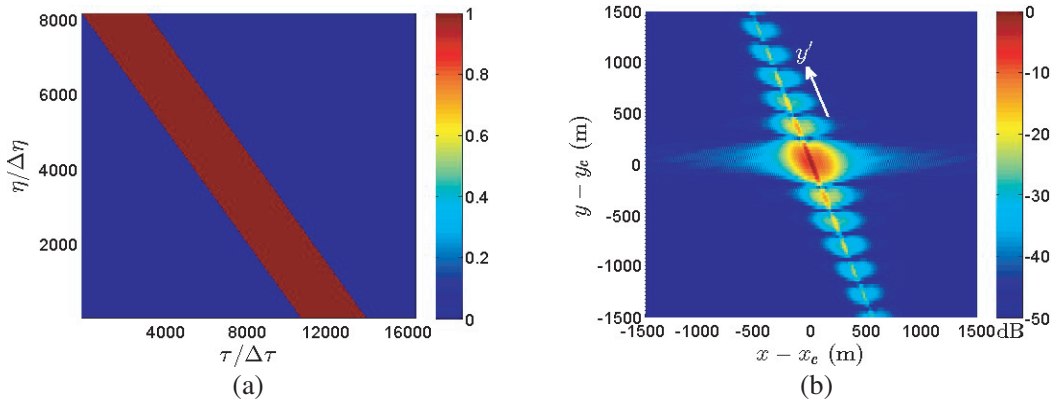


Figure 5. (a) Received signal in τ - η plane and (b) image reconstructed with the conventional FDA, $N_r = 16,384$, $N_a = 8,192$.

Figure 6(a) shows the received signal in the τ' - η' plane, computed by using Eq. (4), and Fig. 6(b) shows the image reconstructed with the proposed method. The number of range samples is reduced to $N'_r = 4,096$, which is large enough to store the received baseband signal after rotation; and the number of azimuth samples remains as $N'_a = 8,192$. The choice of these two sampling numbers is called scheme A.

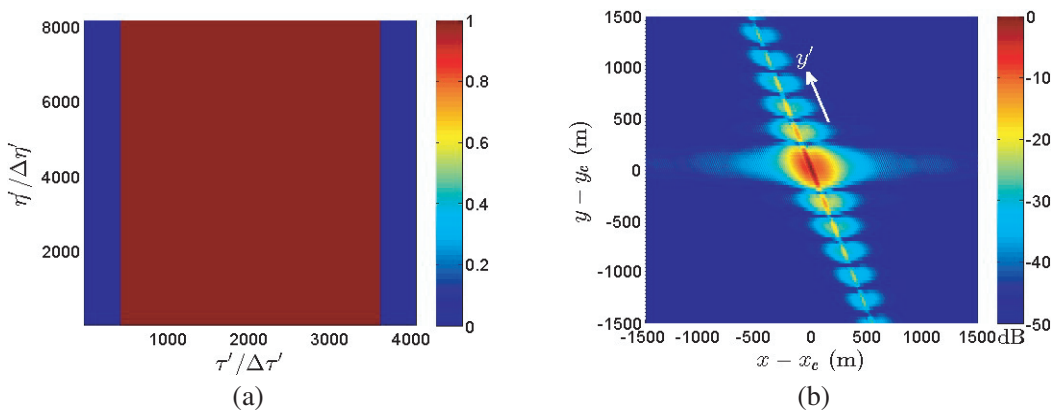


Figure 6. (a) Received signal in τ' - η' plane and (b) image reconstructed with the proposed method under scheme A, $N'_r = 4,096$, $N'_a = 8,192$.

Figures 7(a) and 7(b) show the profiles along x and y' axes, respectively, extracted from the images shown in Figs. 5(b) and 6(b). The image reconstructed with the proposed method has similar quality to that with the conventional FDA because the lengths of synthetic aperture are similar.

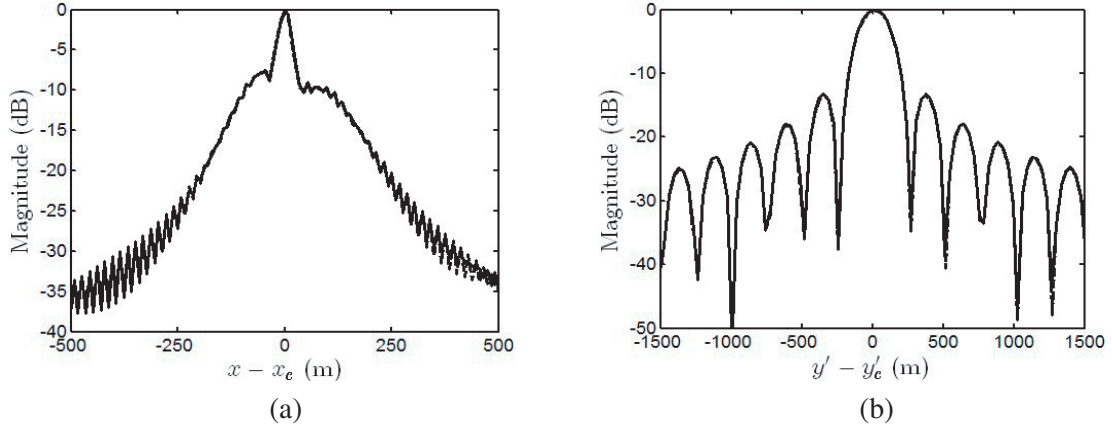


Figure 7. Image profiles along (a) x axis and (b) y' axis, extracted from Fig. 5(b) (---) and Fig. 6(b) (—).

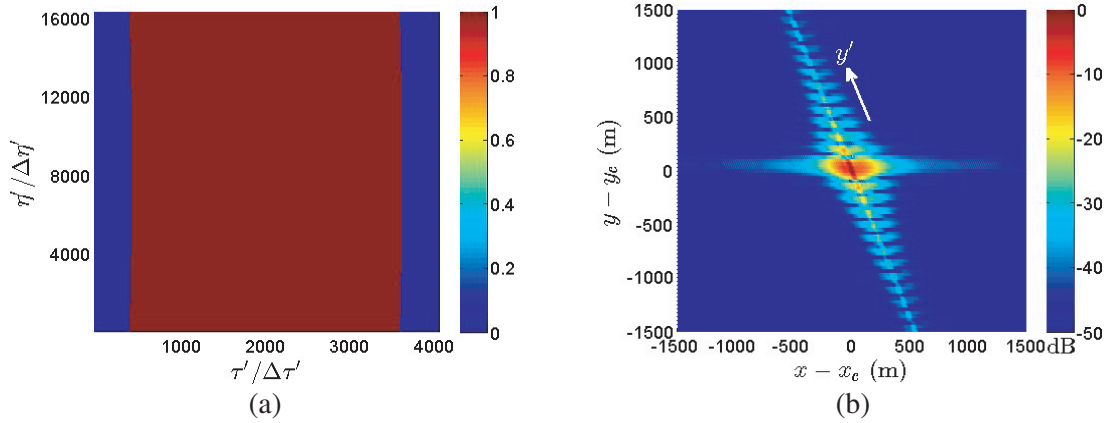


Figure 8. (a) Received signal in τ' - η' plane, and (b) image reconstructed with the proposed method under scheme B, $N'_r = 4,096$, $N'_a = 16,384$.

A second set of sampling numbers, $N'_r = 4,096$ and $N'_a = 16,384$, are chosen and called scheme B. The number of range samples is the same as that in scheme A, but that of the azimuth samples is doubled. The NOMs and memory required under scheme B is larger than that under scheme A because N'_a of the former is twice that of the latter.

Figure 8(a) shows the received signal in the τ' - η' plane, computed by using Eq. (4), and Fig. 8(b) shows the image reconstructed with the proposed method. The number of range samples required by the proposed method is only a quarter that required by the conventional FDA. The number of azimuth samples applied in the proposed method is twice that of the conventional FDA. The reconstructed image appears to have finer spatial resolution in the y' direction because the synthetic aperture length is doubled.

Figures 9(a) and 9(b) show the profiles along x and y' axes, respectively, extracted from the images shown in Figs. 5(b) and 8(b).

Table 4 lists the performance indices of the reconstructed images in event E_1 . The spatial resolution is characterized by the impulse response width (IRW) of a point target. The images reconstructed with the conventional FDA and the proposed method under scheme A are similar. However, the proposed method under scheme A takes only 33% of NOMs and 25% of memory as compared to the conventional FDA. The spatial resolutions in the x direction with the conventional FDA and the proposed method, under both schemes, are similar; and the spatial resolution in the y' direction with the proposed method under scheme B is about half that with the conventional FDA. The proposed method under scheme

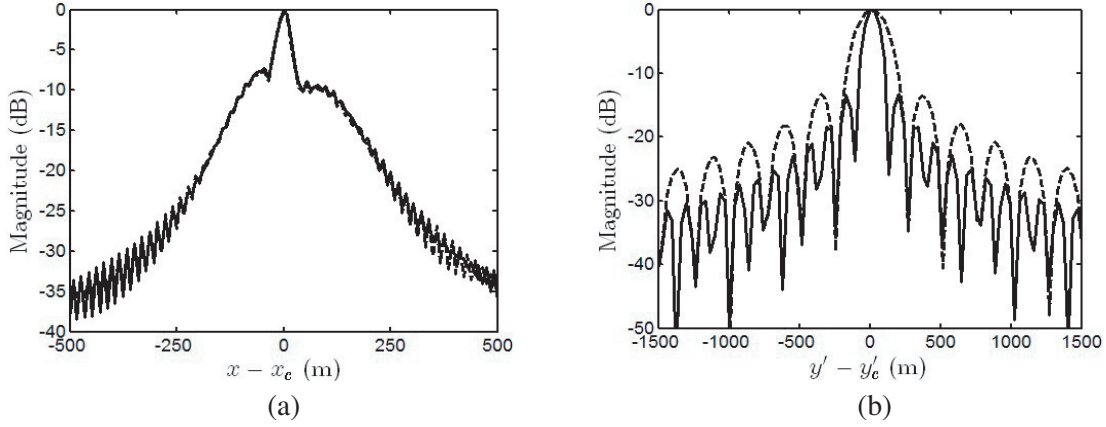


Figure 9. Image profiles along (a) x axis and (b) y' axis, extracted from Fig. 5(b) (---) and Fig. 8(b) (—).

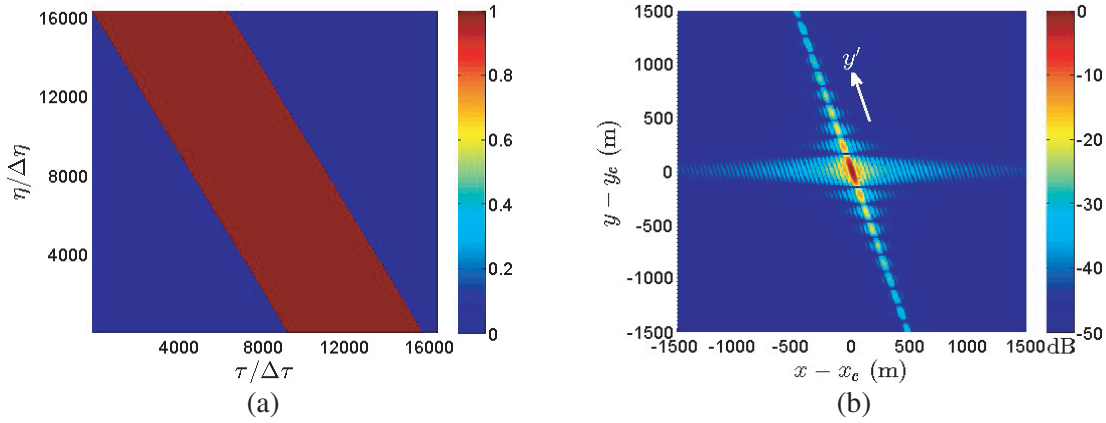


Figure 10. (a) Received signal in τ - η plane and (b) image reconstructed with the conventional FDA, $N_r = 16,384$, $N_a = 16,384$.

B takes 205% of NOMs and twice memory as compared to the proposed method under scheme A. However, the former takes only 67% of NOMs and one half of memory as compared to the conventional FDA. The proposed method under scheme B turns out to perform better than the conventional FDA in all aspects, including the spatial resolution in y' direction, NOMs and memory. The same approach is applied to the other extreme events (E_2 - E_4), the results are similar to those in event E_1 and hence are not presented.

Table 4. Indices of reconstructed image in event E_1 .

index	conventional	proposed (scheme A)	proposed (scheme B)
IRW _{x} (m)	29.651	29.9558	30.6552
IRW _{y'} (m)	220.0219	222.4984	112.075
PSLR _{y'} (dB)	-13.2704	-13.2437	-13.2968
NOM (million)	15,166	4,932	10,133
memory (GB)	2	0.5	1

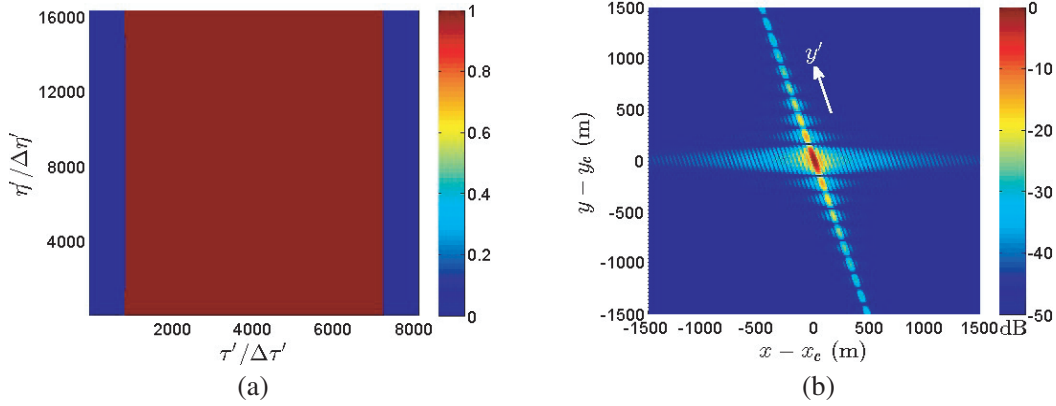


Figure 11. (a) Received signal in $\tau' - \eta'$ plane and (b) image reconstructed with the proposed method, $N'_r = 8,192$, $N'_a = 16,384$.

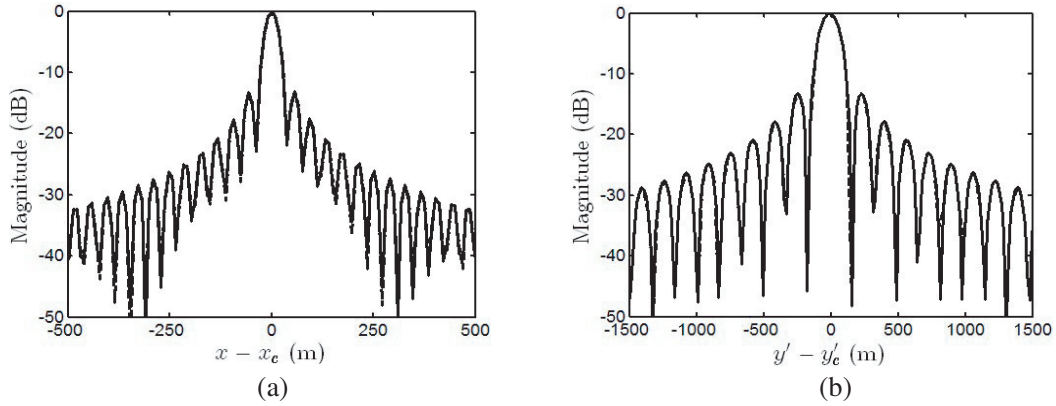


Figure 12. Image profiles along (a) x axis and (b) y' axis, extracted from Fig. 10(b) (---) and Fig. 11(b) (—).

4.2. Event E_5

Figure 10(a) shows the received signal, computed by using Eq. (1), in the $\tau - \eta$ plane. Fig. 10(b) shows the image reconstructed with the conventional FDA, in which local maxima are observed along the x and y' axes.

Figure 11(a) shows the received signal in the $\tau' - \eta'$ plane, computed by using (4), and Fig. 11(b) shows the image reconstructed with the proposed method. The number of range samples is reduced to $N'_r = 8,192$, which is large enough to store the received baseband signal after rotation; and the number of azimuth samples remains as $N'_a = 16,384$.

Figures 12(a) and 12(b) show the profiles along x and y' axes, respectively, extracted from the images shown in Figs. 10(b) and 11(b). The image reconstructed with the proposed method has similar quality to that with the conventional FDA because the lengths of synthetic aperture are similar.

Table 5 lists the performance indices of the reconstructed images in event E_5 . The images reconstructed with the conventional FDA and the proposed method are similar. However, the proposed method takes only 66% of NOMs and one half memory as compared to the conventional FDA.

4.3. Event E_6

Figure 13(a) shows the received signal, computed by using Eq. (1), in the $\tau - \eta$ plane. Fig. 13(b) shows the image reconstructed with the conventional FDA, in which local maxima are observed along x and y axes.

Table 5. Indices of reconstructed image in event E_5 .

index	conventional	proposed
IRW _{x} (m)	33.425	33.2845
PSLR _{x} (dB)	-13.0985	-13.1341
IRW _{y'} (m)	144.074	145.2704
PSLR _{y'} (dB)	-13.2202	-13.2274
NOM (million)	31,407	20,803
memory (GB)	4	2

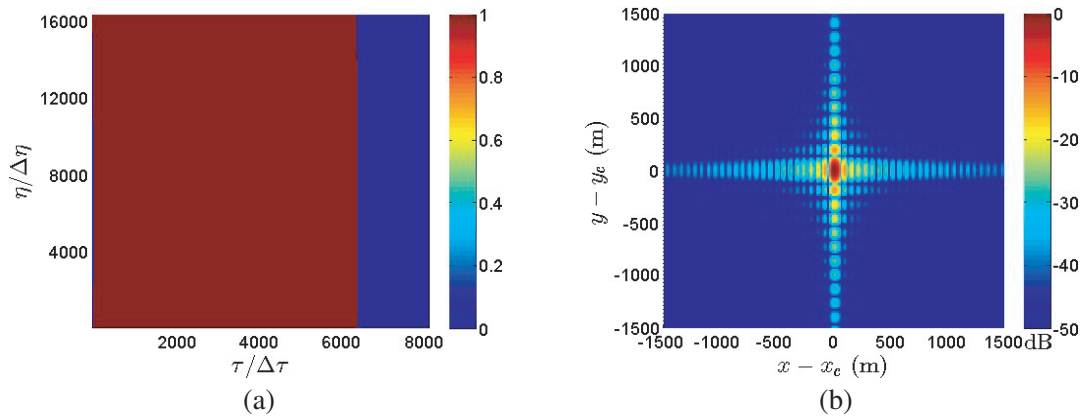


Figure 13. (a) Received signal in τ - η plane and (b) image reconstructed with the conventional FDA, $N_r = 8,192$, $N_a = 16,384$.

Figures 14(a) and 14(b) show the profiles along x and y axes, respectively, extracted from the image shown in Fig. 13(b).

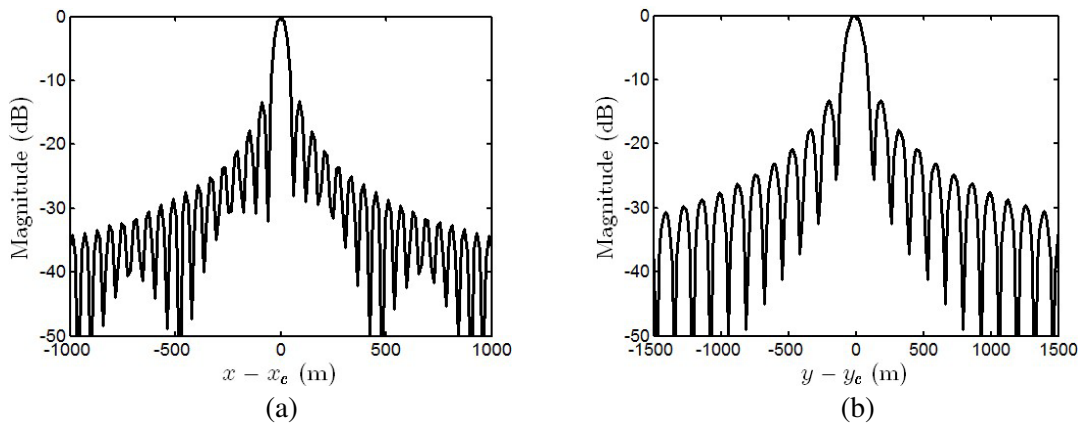


Figure 14. Image profiles along (a) x axis and (b) y axis, extracted from Fig. 13(b).

Table 6 lists the performance indices of reconstructing image in event E_6 . The proposed method does not out-perform the conventional method under low squint angles because the number of range samples in the received signal will not be significantly reduced by rotating the coordinate system.

Table 6. Indices of reconstructed image in event E_6 .

index	conventional
IRW_x (m)	51.3879
$PSLR_x$ (dB)	-13.2813
$IRW_{y'}$ (m)	118.6994
$PSLR_{y'}$ (dB)	-13.2111
NOM (million)	15,167
memory (GB)	2

5. CONCLUSION

Two HEO satellites in a Tundra orbit are envisioned for SAR imaging, which are capable of providing a complete coverage over high-latitude areas. The received baseband signal is rotated in the time domain to significantly reduce the required memory storage. The conventional FDA is also modified to be compatible with the coordinate rotation. Six events with a wide range of squint angles are chosen to evaluate the efficacy of the proposed algorithms. The simulation results confirm the efficacy of the proposed method in terms of spatial resolution, computational load and memory size.

ACKNOWLEDGMENT

This work is partly sponsored by the Ministry of Science and Technology, Taiwan, R.O.C., under contract MOST 105-2221-E-002-035.

REFERENCES

1. Velde, R. V. D., M. S. Salama, O. A. Eweys, J. Wen, and Q. Wang, "Soil moisture mapping using combined active/passive microwave observations over the east of the Netherlands," *IEEE J. Select. Topics Appl. Earth Observ. Remote Sensing*, Vol. 8, No. 9, 4355–4372, Sep. 2015.
2. Reiche, J., C. M. Souza, D. H. Hoekman, J. Verbesselt, H. Persaud, and M. Herold, "Feature level fusion of multi-temporal ALOS PALSAR and landsat data for mapping and monitoring of tropical deforestation and forest degradation," *IEEE J. Select. Topics Appl. Earth Observ. Remote Sensing*, Vol. 6, No. 5, 2159–2173, Oct. 2013.
3. Lucas, R., et al., "An evaluation of the ALOS PALSAR L-band backscatter above ground biomass relationship Queensland, Australia: Impacts of surface moisture condition and vegetation structure," *IEEE J. Select. Topics Appl. Earth Observ. Remote Sensing*, Vol. 3, No. 4, 576–595, Dec. 2010.
4. Zhao, B., Y. Han, W. Gao, Y. Luo, and X. Han, "A new imaging algorithm for geosynchronous SAR based on the fifth-order Doppler parameters," *Progress In Electromagnetics Research B*, Vol. 55, 195–215, 2013.
5. Hu, C., Z. Liu, and T. Long, "An improved CS algorithm based on the curved trajectory in geosynchronous SAR," *IEEE J. Select. Topics Appl. Earth Observ. Remote Sensing*, Vol. 5, No. 3, 795–808, Jun. 2012.
6. Li, D.-X., M.-Q. Wu, Z.-Y. Sun, F. He, and Z. Dong, "Modeling and processing of two-dimensional spatial-variant geosynchronous SAR data," *IEEE J. Select. Topics Appl. Earth Observ. Remote Sensing*, Vol. 8, No. 8, 3999–4010, Aug. 2015.
7. Hu, C., Y. Tian, T. Zeng, T. Long, and X. Dong, "Adaptive secondary range compression algorithm in geosynchronous SAR," *IEEE J. Select. Topics Appl. Earth Observ. Remote Sensing*, Vol. 9, No. 4, 1397–1413, Apr. 2016.

8. Hu, C., T. Long, Z. Liu, T. Zeng, and Y. Tian, "An improved frequency domain focusing method in geosynchronous SAR," *IEEE Trans. Geosci. Remote Sensing*, Vol. 52, No. 9, 5514–5528, Sep. 2014.
9. Ding, Z., B. Shu, W. Yin, T. Zeng, and T. Long, "A modified frequency domain algorithm based on optimal azimuth quadratic factor compensation for geosynchronous SAR imaging," *IEEE J. Select. Topics Appl. Earth Observ. Remote Sensing*, Vol. 9, No. 3, 1119–1131, Mar. 2016.
10. Rodon, J. R., A. Broquetas, A. M. Guarnieri, and F. Rocca, "A Ku-band geosynchronous synthetic aperture radar mission analysis with medium transmitted power and medium-sized antenna," *IEEE Int. Geosci. Remote Sensing Symp.*, 2456–2459, Vancouver, BC, Canada, Jul. 2011.
11. Wood, L., Y. Lou, and O. Olusola, "Revisiting elliptical satellite orbits to enhance the O3b constellation," <https://arxiv.org/ftp/arxiv/papers/1407/1407.2521.pdf>.
12. Ilcev, S. D., *Global Mobile Satellite Communications for Maritime, Land and Aeronautical Applications*, Springer, 2005.
13. Ilcev, S. D., "Highly elliptical orbits (HEO) for high latitudes and polar coverage," *IEEE Int. Crimean Conf. Microwave Telecom. Tech.*, 396–399, Sevastopol, Crimea, Ukraine, Sep. 2010.
14. Cavallaro, G., D. Pham-Minh, and M. Bousquet, "HEO constellation design for tactical communications," *IEEE Euro. Conf. Satellite Telecom.*, Toulouse, France, Oct. 2012.
15. Tsimbal, M. and S. Panko, "Features of the HEO satellite communication systems," *IEEE Int. Siberian Conf. Control Commun.*, Omsk, Russia, May 2015.
16. Agrawal, B. N., "High latitude communications satellite," <http://digitalcommons.usu.edu/cgi/viewcontent.cgi?article=2770&context=smallsat>.
17. Chen, P.-C. and J.-F. Kiang, "An improved range-Doppler algorithm for SAR imaging at high squint angles," *Progress In Electromagnetics Research M*, Vol. 53, 41–52, 2017.